Mutations in *TUBB4B* Cause a Distinctive Sensorineural Disease

Romain Luscan,[1,16] Sabrina Mechaussier,[2,16] Antoine Paul,[1] Guoling Tian,[3] Xavier Gérard,[2] Sabine Defoort-Dellhemmes,[4] Natalie Loundon,[5] Isabelle Audo,[6] Sophie Bonnin,[7] Jean-François LeGargasson,[8] Julien Dumont,[9] Nicolas Goudin,[10] Meriem Garfa-Traoré,[10] Marc Bras,[11] Aurore Pouliet,[12] Bettina Bessières,[13] Nathalie Boddaert,[14] José-Alain Sahel,[6] Stanislas Lyonnet,[1] Josseline Kaplan,[2] Nicholas J. Cowan,[3] Jean-Michel Rozet,[2,*] Sandrine Marlin,[1,15,*] and Isabelle Perrault[2]

Leber congenital amaurosis (LCA) is a neurodegenerative disease of photoreceptor cells that causes blindness within the first year of life. It occasionally occurs in syndromic metabolic diseases and plurisystemic ciliopathies. Using exome sequencing in a multiplex family and three simplex case subjects with an atypical association of LCA with early-onset hearing loss, we identified two heterozygous mutations affecting Arg391 in β-tubulin 4B isotype-encoding (*TUBB4B*). Inspection of the atomic structure of the microtubule (MT) protofilament reveals that the β-tubulin Arg391 residue contributes to a binding pocket that interacts with α-tubulin contained in the longitudinally adjacent αβ-heterodimer, consistent with a role in maintaining MT stability. Functional analysis in cultured cells overexpressing FLAG-tagged wild-type or mutant TUBB4B as well as in primary skin-derived fibroblasts showed that the mutant TUBB4B is able to fold, form αβ-heterodimers, and co-assemble into the endogenous MT lattice. However, the dynamics of growing MTs were consistently altered, showing that the mutations have a significant dampening impact on normal MT growth. Our findings provide a link between sensorineural disease and anomalies in MT behavior and describe a syndromic LCA unrelated to ciliary dysfunction.

Tubulins are the subunits of microtubules (MTs), dynamic polymers that participate in a striking variety of essential cellular functions. Eight α- and nine β-tubulin isotypes are encoded in humans, and there is compelling evidence that their tissue-specific expression patterns and post-translational modifications contribute to the generation of functionally specialized MTs.[1] Mutations in tubulin isotypes have been implicated in a wide and overlapping range of brain malformations collectively known as the tubulinopathies (see GeneReviews in Web Resources). Hitherto, no mutations in *TUBB4B* (encoding the β-tubulin 4B isotype) (MIM: 602660) have been associated with any human disease. Here, we report that monoallelic *TUBB4B* mutations cause a severe neurodegenerative condition of the retina known as Leber congenital amaurosis (LCA), associated with sensorineural hearing loss (SHL).

LCA (MIM: PS204000) is a group of inherited photoreceptor-neuron degenerative diseases that results in severe early-onset visual dysfunction.[2] It typically presents as an autosomal-recessive isolated ocular anomaly without systemic involvement. Diseases involving sensorineural hearing loss (SHL) are essentially monogenic non-syndromic conditions ascribable to inner-ear cell dysfunction (see Hereditary Hearing loss Homepage in Web Resources). The association of a degenerative disease of the retina with SHL is typically seen in multi-tissue syndromic disorders, in particular in metabolic disorders and ciliopathies.[3] The specific association of the two anomalies is known as Usher syndrome (MIM: PS276900), but SHL has been reported in some individuals with retinal degeneration due to *RPGR* (MIM: 312610) mutations.[4] In Usher syndrome, as in individuals with *RPGR* mutations, the retinal disease differs from LCA by a later onset and a less severe visual deficiency.

We identified five individuals from four families with a previously unreported association of LCA and early-onset SHL (families 1–4; Figure 1) and performed whole-exome sequencing (WES) to resolve these uncommon cases. WES informed consent was obtained from all participating individuals, and the study was approved by the Comité de Protection des Personnes "Ile-De-France II." WES datasets were

[1]Laboratory of Embryology and Genetics of Human Malformation, INSERM UMR1163, Institute of Genetic Diseases, *Imagine* and Paris Descartes University, 75015 Paris, France; [2]Laboratory of Genetics in Ophthalmology (LGO), INSERM UMR1163, Institute of Genetic Diseases, *Imagine* and Paris Descartes University, 75015 Paris, France; [3]Department of Biochemistry & Molecular Pharmacology, NYU Langone Medical Center, New York, NY 10016, USA; [4]Service d'Exploration de la Vision et Neuro-ophtalmologie, Pôle d'Imagerie et Explorations Fonctionnelles, CHRU de Lille, Hôpital Roger Salengro, 59000 Lille, France; [5]Pediatric ENT Department, Hôpital Necker-Enfants Malades, APHP and Paris Descartes University, 75015 Paris, France; [6]Centre Hospitalier National d'Ophtalmologie des Quinze-Vingts, 75012 Paris, France; [7]Ophthalmology Department, Hôpital Lariboisière, APHP and Paris Diderot University, 75010 Paris, France; [8]Visual Exploration Department, Hôpital Lariboisière, APHP, Paris, Diderot University, 75010 Paris, France; [9]Cell Division and Reproduction, Institut Jacques Monod, CNRS, University Paris Diderot, 75013 Paris, France; [10]Cell Imaging Core Facility of the Structure Fédérative de Recherche Necker INSERM US24/CNRS UMS3633 *Imagine* and Paris Descartes University, 75015 Paris, France; [11]Bioinformatics Platform, *Imagine* and Paris Descartes University, 75015 Paris, France; [12]Genomics Platform, *Imagine* and Paris Descartes University, 75015 Paris, France; [13]Unité d'Embryo-foetopathologie, Hôpital Necker-Enfants Malades, APHP and Paris Descartes University, 75015 Paris, France; [14]Department of Pediatric Radiology, Hôpital Necker-Enfants Malades, APHP, Paris, Descartes University, 75015 Paris, France; [15]Centre de Référence des Surdités Génétiques, Genetic Department, Hôpital Necker-Enfants Malades, APHP and Paris Descartes University, 75015 Paris, France
[16]These authors contributed equally to this work
*Correspondence: jean-michel.rozet@inserm.fr (J.-M.R.), sandrine.marlin@aphp.fr (S.M.)
https://doi.org/10.1016/j.ajhg.2017.10.010.

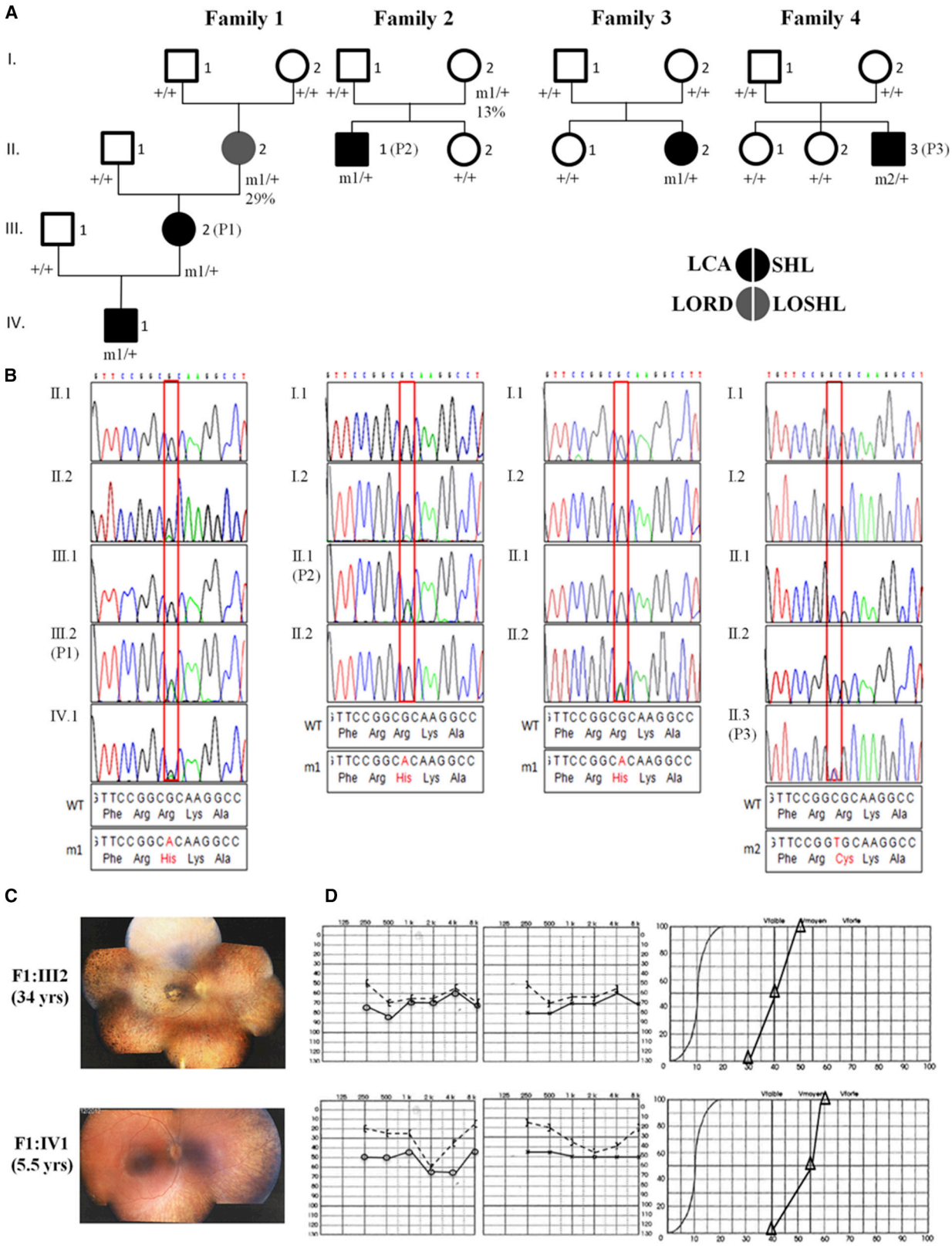

Figure 1. Heterozygous *TUBB4B* Substitutions Affecting Arg391 Cause LCA with Hearing Deficiency
(A) Pedigrees of families and segregation analysis of the mutations. m1, c.1172G>A (p.Arg391His); m2, c.1171C>T (p.Arg391Cys); +, wild-type allele. P1, P2, and P3 are affected individuals whose fibroblasts were analyzed. The percentage below the genotype of individuals I2 in families 1 and 2 shows the relative abundance of mutant reads in genomic DNA from lymphocytes.
(B) Sanger sequence traces around the mutation are shown below the corresponding pedigree.

(legend continued on next page)

generated from individuals II1, II2, III2, and IV1 in family 1 and from the index case subject and his/her parents in families 2–4. Sequencing, image analysis, base calling, and genetic variation annotation were performed as described previously.[5] WES coverage and read-depth were consistent with a high degree of base calling confidence (Table S1). Sequence variants were filtered according to the pedigree structure using the *Imagine* pipeline, POLYWEB.

In family 1, the index case subject (IV1) and his mother (III2) were both affected, supporting a dominant transmission of sensory symptoms. The maternal grandmother (II2) was known to have SHL since her 30s but she did not complain of visual problems. Variants with a minor allele frequency (MAF) exceeding 0.01% were filtered out. Analysis of WES datasets driven by the hypothesis of the occurrence of a *de novo* mutation in a grandparental gamete, transmitted in a dominant manner from III2 to IV1, identified no variant (Table S2). In contrast, considering the transmission of the disease through the deaf maternal grandmother based on the hypothesis of a single disease with variable symptomatic expression, we identified 40 unreferenced or extremely rare heterozygous changes (Table S2). None of them affected a gene involved in eye or ear diseases, except for the unreferenced and likely damaging c.1771T>C (p.Cys591Arg [GenBank: NM_201253.2]) missense substitution identified in *CRB1* (Table S2). Approximately 200 *CRB1* mutations are referenced in the Human Gene Mutation Database. All but one of them cause recessive LCA or retinitis pigmentosa 12 (RP12 [MIM: 600105]). The p.Val162Met substitution within the fourth EGF-like domain has been reported in a unique family with dominant pigmented paravenous chorioretinal atrophy (PRCA [MIM: 172872]), an unusual retinal degeneration characterized by accumulation of pigmentation along retinal veins.[6] By analogy with other dominant retinal diseases caused by mutations in EGF-like domains of other proteins, the uncommon heredity and presentation associated with the p.Val162Met substitution were ascribed to its localization. The localization of the p.Cys591Arg substitution in the laminin G domain involved in several LCA/RP12 missense mutations (HGMD: CM124913, HM0648, HM060031, CM130790, CM043269, CM040711) and the retinal presentation in the mother and her son both differ strikingly from PRCA. These observations argue strongly against the involvement of this gene in the disease in family 1. Of the 38 of the remaining variants, 37 were dismissed because (1) they had high probabilities to be benign and/or they were detected in individuals with no overlapping symptoms in our in-house WES database (*DejaVu,* > 10,000 exomes) (32/38) or (2) they were detected by Sanger sequencing of the DNA of the asymptomatic great-grandparents (I1 or I2, Figure 1) (6/38) (Table S2). The only variant which circumvented filtering was the unreferenced *TUBB4B* c.1172G>A (p.Arg391His [GenBank: NM_006088.5]) substitution predicted to be damaging by PolyPhen-2, SIFT, and MutationTaster (Table S2). This change drew our attention because of a reduced number of variant reads produced from the deaf maternal grandmother's DNA (29% versus 50% of reads produced from the index case subject and his mother's DNAs). This observation suggested a mosaicism that was confirmed by PCR-based deep next-generation sequencing of *TUBB4B* exon 4 (570/1,956 reads generated from the maternal grandmother's DNA versus 1,063/2,215 from the mother's DNA) (Table S3). Consistent with these data, the variant was undetected in the maternal great-grandparents' (I1, I2) DNA, as determined by Sanger sequencing (primer sequences available in Table S4).

Interestingly, inspection of our *DejaVu* database identified the *TUBB4B* c.1172G>A variant in 3 out of more than 10,000 individuals: the index case subjects of families 2 and 3 and the mother in family 2. These individuals carried 50% and 13% of mutant reads, respectively. Deep sequencing analysis were consistent with WES data (Table S3), supporting mosaicism and *de novo* mutational events, respectively. WES datasets were further analyzed in a search for ultra-rare likely damaging *de novo* dominant and rare recessive (MAF < 0.001 and 0.01, respectively) variants, absent in heterozygosity, homozygosity, or hemizygosity (depending on the genetic model) in individuals with no overlapping symptoms (*DejaVu* database). In family 2, this filtering strategy pointed to four genes—*GUCY1B3* (MIM: 139397), *MLST8* (MIM: 612190), *MUC16* (MIM: 606154), and *CDK16* (MIM: 311550)—none of which had a known role in the eye or ear (the *TUBB4B* variant present in 13% of the reads produced from the mother's DNA was not detected) (Table S2). In families 3 and 4, unique variants circumvented filtering: the *TUBB4B* c.1172G>A change and another *TUBB4B* unreferenced and likely damaging (PolyPhen-2, SIFT, and Mutation Taster) variant affecting the adjacent nucleotide (c.1171C>T [p.Arg391Cys]), respectively (Figure 1 and Table S2). The c.1172G>A and c.1171C>T substitutions were absent in parental DNA as determined by WES and deep sequencing, suggesting a *de novo* event (families 3 and 4, respectively; Figure 1 and Table S3). Familial segregation analysis of the *TUBB4B* c.1172G>A and c.1171C>T mutations with the disease was further confirmed by Sanger sequencing (Figure 1).

(C and D) Representative eye fundus views and audiograms in two individuals with *TUBB4B* substitutions affecting Arg391. The eldest individual's funduscopy image displays features of advanced retinitis pigmentosa with a marked reduction in the caliber of retinal vessels, generalized choroid atrophy, marked macular rearrangements, and numerous pigmentary deposits in the periphery. The fundus of the youngest individual displays similar abnormalities, although to a much lesser extent (C). Left and right ear pure-tone audiograms of the two individuals displaying moderate symmetric hearing loss (left and central panels, respectively). Vocal audiograms (right panels) are consistent with pure-tone traces, suggesting that the two individuals have endocochlear deafness (D).

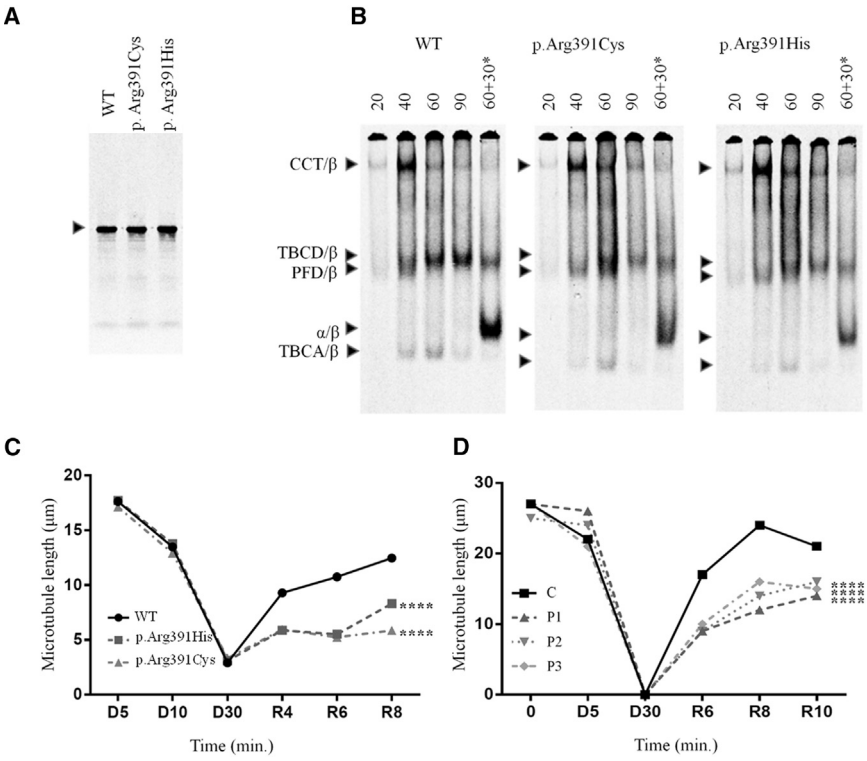

Figure 2. Functional Analysis of *TUBB4B* Mutations *In Vitro*, in Cultured Cells, and in Skin Fibroblasts

(A and B) Folding *in vitro*. Plasmids encoding full-length TUBB4B (wild-type or containing the mutations shown) were expressed in rabbit reticulocyte lysate containing ^{35}S-methionine.

(A) Labeled reaction products analyzed by SDS-PAGE. Arrow: migration position of β-tubulin.

(B) Kinetic analysis by native 4.5% PAGE of labeled reaction products done for the times shown (in min).

In each panel, the right-hand track (marked with an asterisk) shows reactions chased with unlabeled native αβ-tubulin heterodimers, included so as to drive the heterodimer assembly reaction. Arrows (top to bottom): CCT/β-tubulin binary complex, TBCD/β-tubulin folding intermediate, prefoldin (PFD)/β-tubulin binary complex, αβ-tubulin heterodimer, and TBCA/β-tubulin folding intermediate.

(C and D) Depressed MT growth rates in transfected COS7 cells (C) and in patient-derived skin fibroblasts (D) following recovery from cold-induced depolymerization.

See Figures S2 and S3 for methods and statistical analyses.

The folding and assembly of the αβ-tubulin heterodimer depends on the concerted action of several molecular chaperones. Nascent tubulin polypeptides are first recognized and stabilized by the heterohexameric chaperone prefoldin, which delivers its bound target protein to the cytosolic chaperonin CCT.[7] The latter provides a sequestered chamber in which the target protein can partition on a productive folding pathway via multiple ATP-dependent iterations of binding and release from the chaperonin's internal surfaces. Quasi-native tubulins discharged from the chaperonin interact with a series of downstream tubulin-specific chaperones termed TBCA-TBCE that act in concert as an αβ-tubulin heterodimer assembly nanomachine controlled by hydrolysis of β-tubulin-bound GTP.[8,9] To determine the influence of the mutations we discovered on the chaperone-dependent αβ-heterodimer assembly pathway, we analyzed the products of coupled *in vitro* transcription/translation reactions driven by full-length cDNA constructs encoding wild-type and mutant forms of TUBB4B.[9] As expected for single amino acid substitutions, we found that the wild-type and mutant proteins were transcribed and translated with the same efficiency (Figure 2A). However, kinetic analysis of these reactions done under native conditions revealed some differences with respect to wild-type, most conspicuously in the diminished yield of the TBCD/β-tubulin folding intermediate from t = 60 mins onward and of *de novo* folded αβ-tubulin heterodimers in the case of TUBB4B p.Arg391Cys and p.Arg391His (Figure 2B). A reduction in the yield of TBCD/β-tubulin implies a reduced stability or a reduced affinity of CCT-generated mutant-containing folding intermediates for TBCD, in either case leading to a reduced relative yield of mutant-containing αβ-heterodimers (quantitated from 6 independent experiments, Figure S1). There is also a possibility that the production of mutant αβ-heterodimers might have a dominant-negative effect on overall *de novo* heterodimer production.

Typically, different tubulin isotypes can freely intermingle into mosaic MTs upon expression in cultured cells.[10] To determine the ability of the p.Arg391His and p.Arg391Cys substitutions to incorporate into the MT lattice *in vivo*, we co-transfected COS7 cells with wild-type and mutant pcDNA3.1-TUBB4B-C-(K)DYK constructs and a pCAGG-GFP plasmid. FLAG-tagged mutant and wild-type TUBB4B protein levels were similar as determined by computed-densitometry analysis of western blots using anti-FLAG and anti-GFP antibodies (Figure S2A). Immune staining using an end-binding 1 (EB1) protein antibody to label the +ends of polymerizing protofilaments[11] showed comparable MT lattices in cells overexpressing mutant and wild-type TUBB4B (Figure S2B). Consistent with our folding data (Figures 2B and S1), these experiments show that the mutant TUBB4B proteins were able to fold, form αβ dimers, and co-assemble into the endogenous MT lattice. While the mutations did not alter the cold-driven depolymerization of these MT lattices, we found that they had a significant impact on MT repolymerization dynamics (Figures 2C, 2D, and S2B). We conclude that the p.Arg391His and p.Arg391Cys substitutions have a dampening effect on normal MT growth.

We obtained and analyzed skin-derived fibroblasts from three affected individuals (F1:III2, F2:II1, F4:II3) and three

control subjects (C1–C3). RT-qPCR analysis using *TUBB4B*-specific primers showed that cells from control subjects and affected individuals expressed similar mRNA amounts (Figure S3A). We were unable to analyze TUBB4B protein levels due to the very high degree of homology among tubulin isotypes and the absence of any non-cross-reacting isotype-specific antibodies. Fibroblasts from the affected individuals had unremarkable steady-state MT lattices and displayed similar MT depolymerization dynamics upon either cold exposure (which induces MT depolymerization [Figures 2D and S3B]) or by incubation at 37°C with the MT-depolymerizing drug nocodazole (Figure S4). However, as in the case of transfected COS7 cells, fibroblasts from affected individuals showed dramatically diminished MT growth rates (Figures 2D, S2B, and S3C).

Inspection of the atomic structure of β-tubulin[12,13] within a MT protofilament shows that Arg391 and the adjacent Arg390 and Lys392 residues form a binding pocket that interacts with α-tubulin in the longitudinally adjacent tubulin αβ-heterodimer.[14] The diminished MT growth rates found in cells expressing the *TUBB4B* mutations suggests that substitution of p.Arg391 in the H11 helix of β-tubulin by either a histidine or a cysteine residue destabilizes hydrophobic interactions between the β-tubulin H11′ helix and the T7 loop and H8 helix of α-tubulin contained in the adjacent αβ-heterodimer[15] (Figure S5). This predicted destabilization is consistent with the observed effect of the p.Arg391 variant on the dynamics of MT growth.

The anomalous MT polymerization rates in fibroblasts from affected individuals had no impact on cell proliferation as determined by an automated live cell proliferation assay (Figure S6), nor was ciliogenesis affected as determined by measuring the abundance and size of acetylated α-tubulin-stained cilia axonemes in serum-starved cells (Figures S7A and S7B). Ciliary trafficking, assessed by immune staining of the centrosomal CEP290 and the intraflagellar IFT 20, 25, 81, and 140 proteins, was also unaffected (Figure S8).

All individuals carrying the c.1171C>T or c.1172G>A mutations except F1:II2 and F2:I2 had early-onset and severe visual and auditory symptoms (Table 1). The youngest (F1:IV1, F3:II2, F4:II3, ages < 10 years) presented with retinal disease consistent with the rod-cone dystrophy subtype of LCA or LCA-type 2 (Table 1).[16] No early ophthalmologic data were available for F1:III2 and F2:II1 (aged 34 and 31 years, respectively). However, current clinical data (in particular the retinitis pigmentosa appearance of the fundus) were consistent with advanced LCA-type 2 (Table 1 and Figures 1C and S9). All individuals had high hypermetropia, which is atypical in LCA-type 2.[16] Hearing defects were diagnosed from birth to age 8 years regardless of the mutation (Table 1 and Figures 1D and S10). All individuals had normal neuro-psychomotor development, and a cerebral MRI available for F4:II3 at age 2 months showed no anomalies (Figure S11).

F1:II2, aged 61 and carrying the c.1172G>A mutation on 29% of *TUBB4B* alleles, had SHL in her 30s and a history of highly asymmetric hypermetropia with left eye amblyopia, although she claimed she had no visual problems. Upon examination she presented with hypermetropia of +6 and +9 diopters and her best corrected visual acuities were 20/20 and 20/29 (right and left eye, respectively; Table 1). Interestingly, fundus examination and optic coherence tomography (OCT) showed objective signs of retinal degeneration (Figure S9), but her photopic and scotopic electroretinograms (ERGs) were normal (Figure S12). F2:I2, aged 57 and carrying the same mutation on 13% of *TUBB4B* alleles, had no auditory symptoms upon examination. She did not complain of visual problems and had no sign of retinal involvement upon detailed ophthalmological examination, including funduscopy, OCT, and ERG recordings.

Evidence of mosaicism in blood cells of the two women, and presumably in the ear and retina of F1:II2 presenting with mild retinal disease and SHL, is consistent with a somatic mosaicism. On the other hand, transmission of the disease through these women to the descendant demonstrates that the mutation affects the germline. Such a situation is typically seen when the mutation occurs very early in development. Interestingly, the two *TUBB4* mutations change a cytosine involved in CpG dinucleotides (+ and – strands, respectively) into a thymine. It is likely that the mutation occurred by the spontaneous deamination of the methylated versions of these cytosines, a mechanism known to contribute to nucleotide hypermutability.[17] The eye and ear involvement in F1:II2 suggest mosaicism in the retinal and cochlear cells of the individual with the highest proportion of mutant-bearing blood cells, questioning the correlation between mosaic ratio and disease expression. The *TUBB4B*-related sensorineural phenotype raises the question of the mechanisms involved in cell-type-specific effects. While most tubulin mutations causing tissue- and cell-type-specific pathologies occur in broadly expressed isotypes,[18] mutations in *TUBB1* (MIM: 612901),[19] *TUBB3* (MIM: 602661),[20] and *TUBB8* (MIM: 616768)[21] cause symptoms that correlate with tissue-specific expression. We analyzed the abundance of *tubb4b* mRNA by RT-qPCR in a spectrum of mouse tissues to assess tissue-specific expression. *tubb4b* mRNA was detected in all analyzed embryonic and adult tissues, including the retina and cochlea. We note that compared to other embryonic and adult tissues, the retina expressed a significantly higher level of *tubb4b* mRNA (Figure S13). This could reflect a specific requirement for TUBB4B in retinal development; however, the low relative expression of *tubb4b* in the cochlea questions the existence of a universal correlation between tissue-specific expression and phenotypic disease.

In summary, we have identified *TUBB4B* mutations as the cause of a previously unreported autosomal-dominant syndrome manifesting as early-onset and severe photoreceptor and cochlear cell loss. Our data provide a link between a sensorineural disease and anomalies in MT behavior and describe an early-onset and severe retinal disease with extraocular associated features unrelated to cilia or metabolic dysfunctions. Currently, no means exist to prevent photoreceptor loss in individuals with *TUBB4B*

Table 1. Genotype and Phenotype of Families with *TUBB4B* Mutations

Family	Individual (Age in Years)	Origin	Nucleotide Alteration	Deduced Protein Change	Retinal Disease	Auditory Defects
1	II2 (61)	France	c.1172G>A (mosaic 29%)	p.Arg391His	normal ERG VA 20/20 (RE), 20/29 (LE) hypermetropia +6 (RE), +9 (LE) pigmentary deposits and atrophy in the peripheral retina, peripapillar atrophy, and macular alterations (Figure S9A)	diagnosis at 30 years A: 75/70
1	III2 (P1) (34)	France	c.1172G>A (het)	p.Arg391His	diagnosis at birth nystagmus flat ERG complete blindness photophobia hypermetropia +6 (LRE) thin retinal vessels, salt and pepper appearance of the posterior pole, yellowish peripheral retina with round pigmented spots at the fundus, macular reorganization (30 year; Figure S9A)	diagnosis at 7 years A: 70/70 ABR: 100/65
1	IV1 (6)	France	c.1172G>A (het)	p.Arg391His	diagnosis at birth flat ERG VA 20/63 (LRE) constricted VF hypermetropia +10 (LRE) thin retinal vessels, salt and pepper appearance of the posterior pole, yellowish peripheral retina with round pigmented spots at the fundus (Figure S9A)	diagnosis at birth A: 45/45
2	I2 (64)	Algeria	c.1172G>A (mosaic 13%)	p.Arg391His	asymptomatic	asymptomatic
2	II1 (P2) (31)	Algeria	c.1172G>A (het)	p.Arg391His	diagnosis at 2.5 years nystagmus VA reduced to LP (22yrs) photophobia hypermetropia +8 (LRE) narrowed retinal vessels and a beaten-bronze appearance of retinal periphery with some pigment migration and macular atrophic changes (Figure S9A)	diagnosis at 8 years A: 60/55 ABR: 70/60
3	II2 (6)	France	c.1172G>A (het)	p.Arg391His	diagnosis at 3 years severely altered photopic and scotopic ERG VA 20/40 (LRE) hemeralopia constricted VF hypermetropia +7 thin retinal vessels, dull retina at the fundus (textual description)	diagnosis at 3 years A: 20 drained serous otitis
4	II3 (P3) (9)	Denmark	c.1171C>T (het)	p.Arg391Cys	diagnosis at birth flat ERG VA 20/50 (RE), 20/63 (LE) hemeralopia constricted VF hypermetropia + 8.25 (RE) +8.75 (RE) slightly pale disc, narrowed retinal vessel, pale retinal periphery with bronze-beaten appearance, absence of pigment migration, and perimacular retinal atrophy at the fundus (Figure S9A)	diagnosis at birth A: 50/50 ABR: 60/45 OAE: absent

Segregation analysis confirmed the *de novo* status of the mutation in families 3 and 4 and dominant transmission in families 1 and 2. Abbreviations: ERG, electroretinogram; LE, left eye; RE, right eye; LRE, left and right eyes; LP, light perception; VF, visual field; VA, visual acuity; A, audiogram (HdB level) right ear/left ear; OAE, oto-acoustic emissions; ABR, auditory brainstem evoked response (HdB level).

mutations. However, early identification of hearing loss and early intervention have proven highly important for language development.[22,23] Based on our findings, systematic auditory explorations merit consideration in infants with LCA to provide optimal care to those in need.

Supplemental Data

Supplemental Data include 13 figures and 4 tables and can be found with this article online at https://doi.org/10.1016/j.ajhg.2017.10.010.

Acknowledgments

We are grateful to the families for their participation in the study. This work was supported by "S'entendre," by grants from Retina France to I.P., UNADEV-AVIESAN ITMO MNP (R16073KS) to J.-M.R., FRM (DEQ20160334869) to J.D., and by a grant from the NIH (GM097376) to N.J.C.

Received: July 28, 2017
Accepted: October 25, 2017
Published: November 30, 2017

Web Resources

1000 Genomes, http://www.internationalgenome.org/
Alamut Interpretation Software 2.0 (gateway for Align DGVD, PolyPhen-2, SIFT, SpliceSiteFinder-like, MaxEntScan, NNSPLICE, and Human Splicing Finder), http://www.interactive-biosoftware.com
dbSNP, https://www.ncbi.nlm.nih.gov/projects/SNP/
ExAC Browser, http://exac.broadinstitute.org/
GenBank, https://www.ncbi.nlm.nih.gov/genbank/
GeneReviews, Bahi-Buisson, N., and Cavallin, M. (1993). Tubulinopathies Overview. https://www.ncbi.nlm.nih.gov/books/NBK350554/
Hereditary Hearing loss Homepage, http://hereditaryhearingloss.org/

Human Gene Mutation Database, http://www.hgmd.cf.ac.uk/ac/index.php
I-TASSER, https://zhanglab.ccmb.med.umich.edu/I-TASSER/
NHLBI Exome Sequencing Project (ESP) Exome Variant Server, http://evs.gs.washington.edu/EVS/
OMIM, http://www.omim.org/
UCSF Chimera, http://www.cgl.ucsf.edu/chimera/

References

1. Gadadhar, S., Bodakuntla, S., Natarajan, K., and Janke, C. (2017). The tubulin code at a glance. J. Cell Sci. *130*, 1347–1353.
2. Leber, T. (1869). Ueber Retinitis pigmentosa und angeborene Amaurose. Archiv fur Opthalmologie *15*, 1–25.
3. Mysore, N., Koenekoop, J., Li, S., Ren, H., Keser, V., Lopez-Solache, I., and Koenekoop, R.K. (2014). A review of secondary photoreceptor degenerations in systemic disease. Cold Spring Harb. Perspect. Med. *5*.
4. Zito, I., Downes, S.M., Patel, R.J., Cheetham, M.E., Ebenezer, N.D., Jenkins, S.A., Bhattacharya, S.S., Webster, A.R., Holder, G.E., Bird, A.C., et al. (2003). RPGR mutation associated with retinitis pigmentosa, impaired hearing, and sinorespiratory infections. J. Med. Genet. *40*, 609–615.
5. Gerber, S., Alzayady, K.J., Burglen, L., Brémond-Gignac, D., Marchesin, V., Roche, O., Rio, M., Funalot, B., Calmon, R., Durr, A., et al. (2016). Recessive and dominant de novo ITPR1 mutations cause Gillespie syndrome. Am. J. Hum. Genet. *98*, 971–980.
6. McKay, G.J., Clarke, S., Davis, J.A., Simpson, D.A.C., and Silvestri, G. (2005). Pigmented paravenous chorioretinal atrophy is associated with a mutation within the crumbs homolog 1 (CRB1) gene. Invest. Ophthalmol. Vis. Sci. *46*, 322–328.
7. Vainberg, I.E., Lewis, S.A., Rommelaere, H., Ampe, C., Vandekerckhove, J., Klein, H.L., and Cowan, N.J. (1998). Prefoldin, a chaperone that delivers unfolded proteins to cytosolic chaperonin. Cell *93*, 863–873.
8. Cowan, N.J., and Lewis, S.A. (2001). Type II chaperonins, prefoldin, and the tubulin-specific chaperones. Adv. Protein Chem. *59*, 73–104.
9. Tian, G., and Cowan, N.J. (2013). Tubulin-specific chaperones: components of a molecular machine that assembles the α/β heterodimer. Methods Cell Biol. *115*, 155–171.
10. Lewis, S.A., Gu, W., and Cowan, N.J. (1987). Free intermingling of mammalian beta-tubulin isotypes among functionally distinct microtubules. Cell *49*, 539–548.
11. Dixit, R., Barnett, B., Lazarus, J.E., Tokito, M., Goldman, Y.E., and Holzbaur, E.L. (2009). Microtubule plus-end tracking by CLIP-170 requires EB1. Proc. Natl. Acad. Sci. USA *106*, 492–497.
12. Nogales, E., Wolf, S.G., and Downing, K.H. (1998). Structure of the alpha beta tubulin dimer by electron crystallography. Nature *391*, 199–203.
13. Nogales, E., Whittaker, M., Milligan, R.A., and Downing, K.H. (1999). High-resolution model of the microtubule. Cell *96*, 79–88.
14. Breuss, M.W., Nguyen, T., Srivatsan, A., Leca, I., Tian, G., Fritz, T., Hansen, A.H., Musaev, D., McEvoy-Venneri, J., James, K.N., et al. (2017). Uner Tan syndrome caused by a homozygous TUBB2B mutation affecting microtubule stability. Hum. Mol. Genet. *26*, 258–269.
15. Zhang, R., Alushin, G.M., Brown, A., and Nogales, E. (2015). Mechanistic origin of microtubule dynamic instability and its modulation by EB proteins. Cell *162*, 849–859.
16. Perrault, I., Rozet, J.M., Gerber, S., Ghazi, I., Leowski, C., Ducroq, D., Souied, E., Dufier, J.L., Munnich, A., and Kaplan, J. (1999). Leber congenital amaurosis. Mol. Genet. Metab. *68*, 200–208.
17. Zemojtel, T., Kielbasa, S.M., Arndt, P.F., Chung, H.-R., and Vingron, M. (2009). Methylation and deamination of CpGs generate p53-binding sites on a genomic scale. Trends Genet. *25*, 63–66.
18. Tischfield, M.A., Cederquist, G.Y., Gupta, M.L., Jr., and Engle, E.C. (2011). Phenotypic spectrum of the tubulin-related disorders and functional implications of disease-causing mutations. Curr. Opin. Genet. Dev. *21*, 286–294.
19. Fiore, M., Goulas, C., and Pillois, X. (2017). A new mutation in TUBB1 associated with thrombocytopenia confirms that C-terminal part of β1-tubulin plays a role in microtubule assembly. Clin. Genet. *91*, 924–926.
20. Tischfield, M.A., Baris, H.N., Wu, C., Rudolph, G., Van Maldergem, L., He, W., Chan, W.M., Andrews, C., Demer, J.L., Robertson, R.L., et al. (2010). Human TUBB3 mutations perturb microtubule dynamics, kinesin interactions, and axon guidance. Cell *140*, 74–87.
21. Feng, R., Sang, Q., Kuang, Y., Sun, X., Yan, Z., Zhang, S., Shi, J., Tian, G., Luchniak, A., Fukuda, Y., et al. (2016). Mutations in TUBB8 and human oocyte meiotic arrest. N. Engl. J. Med. *374*, 223–232.
22. Moeller, M.P. (2000). Early intervention and language development in children who are deaf and hard of hearing. Pediatrics *106*, E43.
23. Yoshinaga-Itano, C. (1999). Benefits of early intervention for children with hearing loss. Otolaryngol. Clin. North Am. *32*, 1089–1102.

The American Journal of Human Genetics, Volume *101*

Supplemental Data

Mutations in *TUBB4B* Cause a Distinctive Sensorineural Disease

Romain Luscan, Sabrina Mechaussier, Antoine Paul, Guoling Tian, Xavier Gérard, Sabine Defoort-Dellhemmes, Natalie Loundon, Isabelle Audo, Sophie Bonnin, Jean-François LeGargasson, Julien Dumont, Nicolas Goudin, Meriem Garfa-Traoré, Marc Bras, Aurore Pouliet, Bettina Bessières, Nathalie Boddaert, José-Alain Sahel, Stanislas Lyonnet, Josseline Kaplan, Nicholas J. Cowan, Jean-Michel Rozet, Sandrine Marlin, and Isabelle Perrault

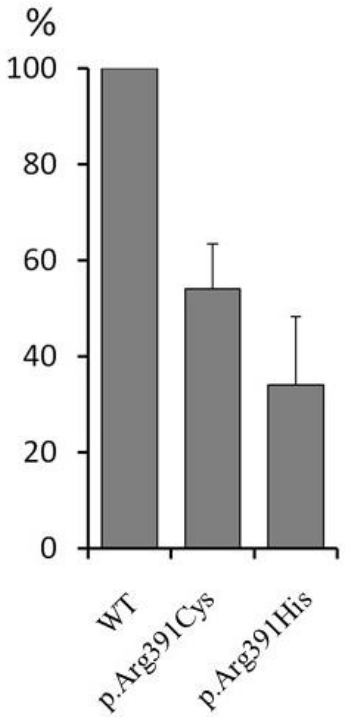

Figure S1. Quantification of ^{35}S-methionine-labeled TUBB4B wild type, p.Arg391Cys and p.Arg391His αβ-tubulin heterodimers produced by in vitro transcription/translation.

Quantification of relative yields of ^{35}S-methionine-labeled TUBB4B wild type (WT), p.Arg391Cys and p.Arg391His αβ-tubulin heterodimers produced by in vitro transcription/translation for 90 mins and chased for a further 30 mins with added depolymerized brain tubulin (see Figure 2B). The yield of WT αβ-tubulin heterodimers is taken as 100%. Data are presented as mean ± SD from six independent reactions, in each case measured using a phosphoimager.

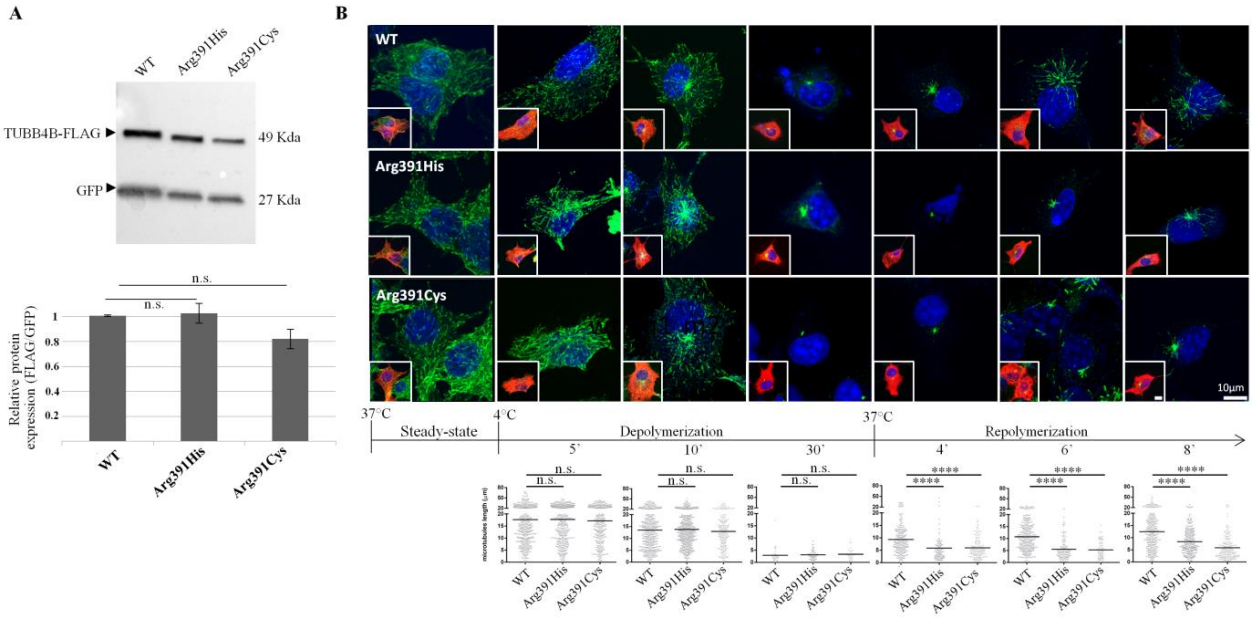

Figure S2. Overexpression of TUBB4B p.Arg391Cys and p.Arg391His affects the polymerization dynamics of COS7 microtubules.

(**A**) Western blot (upper panel) and computed-densitometry (lower panel) analysis of wild-type and mutant FLAG-tagged TUBB4B relative to GFP. COS7 cells were co-transfected with wild-type or mutant FLAG-tagged TUBB4B plasmids (800 ng) and the pCAGGS-GFP plasmid (200 ng; Clontech, California, USA) using the FuGene HD transfection reagent according to the manufacturer's protocol (Promega, Charbonnières-les-Bains, France). After 48 hours, GFP-expressing cells were sorted on a Sony SH800 cell sorter (Sony Biotechnology, San Jose, CA, USA). 50 µg of total protein prepared using RIPA lysis buffer (Life Technologies ThermoFisher Scientific) was resolved on a Mini-ProteanTGX Stain Free 4-20% gel according to the supplier's recommendations (BioRad, Marne la Coquette, France). Proteins were transferred to a PVDF membrane using a RTA transfer kit (BioRad) which was probed with the following primary antibodies: Monoclonal ANTI-FLAG® M2 antibody (Sigma Aldrich, Missouri USA); anti-GFP from mouse $IgG_1\kappa$ (clones 7.1 and 13.1) (Sigma Aldrich) and goat anti-mouse IgG-HRP and goat anti-rabbit HRP secondary antibodies (2 mg/mL, 1:10,000, Abcam, Paris, France). Blots were developed using the Clarity Western ECL and ChemiDoc XRS+ Imaging System (BioRad) and images were acquired and analyzed with Image Lab Software 3.0.1 build 18 (BioRad). The abundance of FLAG relative to GFP was estimated by densitometry using Image Lab Software 3.0.1 build 18. Values are means ± SD of densities from three independent transfection experiments. A t-Student test was used to compare the abundance of FLAG in the different experiments.

(B) Appearance and length of MTs. COS7 cells were transfected with wild-type or mutant FLAG-tagged TUBB4B plasmids as described in (A). After 48 hours, cells were fixed in ice-cold methanol (5 minutes at −20 °C) without further treatment (steady-state MT lattice) or after having been maintained on ice for 5, 10 and 30 min. (MT depolymerization) or for 30 min. prior to incubation at 37°C (MT repolymerization) for 4, 6 and 8 min., respectively. Fixed cells were permeabilized (1 hour, room temperature) and immunostained using mouse Anti-EB1 (1:200, overnight, 4°C, BD Biosciences, Le-Pont-De-Claix, France) and rabbit anti-FLAG (1:2000, overnight, 4°C; Sigma Aldrich) primary antibodies, and alexa fluor 488 donkey anti-mouse or alexa fluor 568 donkey anti-rabbit secondary antibodies (1:1000, 1 hour 37°C, Life Technologies ThermoFisher Scientific). A mounting medium containing 4′,6-diamidino-2-phenylindole (DAPI) (Prolong Gold, Life Technologies ThermoFisher Scientific) was used to label nuclei. Immunofluorescence images were obtained using a Spinning Disk Zeiss microscope (Zeiss, Oberkochen, Germany). Final images were generated using ImageJ (National Institutes of Health, Bethesda, MA, USA). Below each row of images, the individual distance of EB1 relative to the centrosome (determined using Icy software) is plotted as a dot, with the mean distance represented by a horizontal line. Statistical analyses were carried out by analysis of variance (ANOVA) and the PLSD Fisher test. ****: p-value < 0.0001. ; n.s.: non-significant p-value ≥ 0.5.

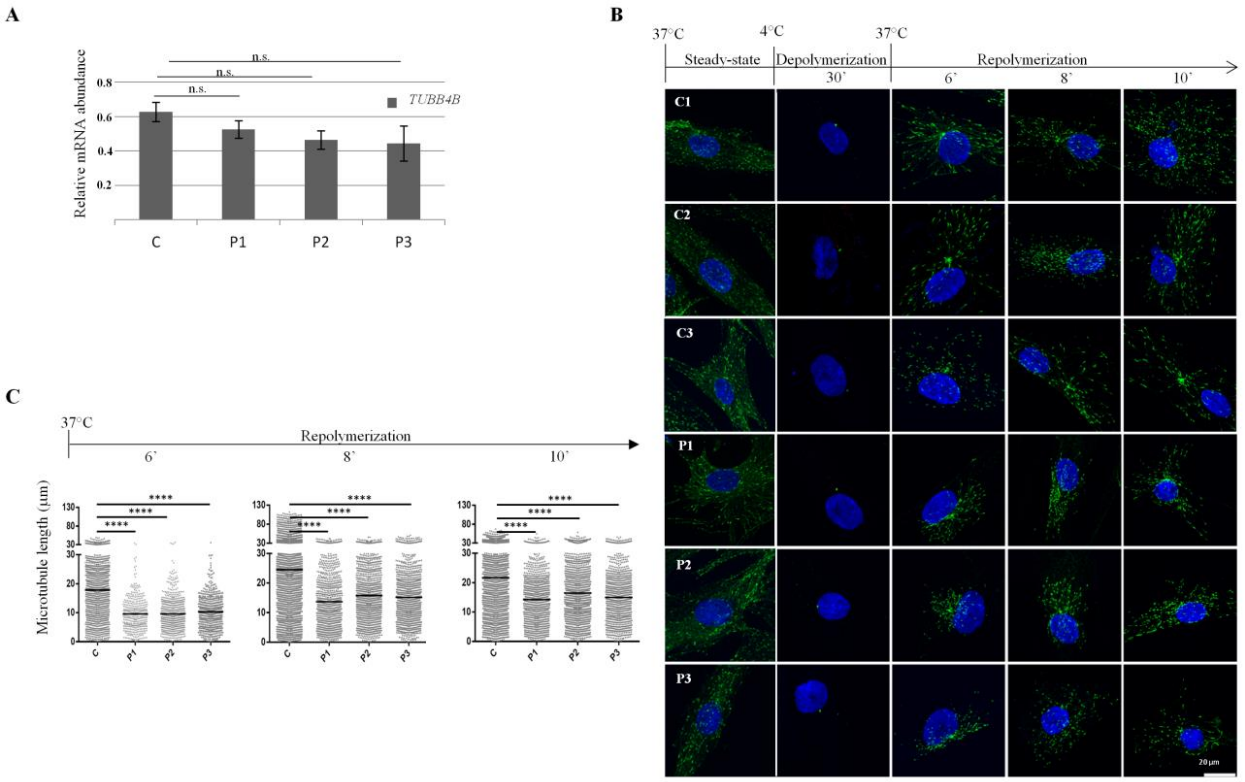

Figure S3. *TUBB4B* c.1172G>A and c.1171C>T mutations affect MT polymerization dynamics in patient fibroblasts.

(**A**) Relative abundance of *TUBB4B* mRNA in control (C) and affected patient-derived (P1, P2, P3) skin fibroblasts. *TUBB4B mRNA* abundance was measured from skin fibroblast RNA as described previously.[1] The *TUBB4B* cDNA was amplified as a 57 bp fragment using exonic primers: (forward, 5'-3') ggcccttcgggcagatctt and (reverse, 5'-3') cagcaccactctgaccgaaa. *B2M* (NM_004048.2), *HPRT1* (NM_000194), *RPLP0* (NM_001002.3) mRNAs and the *ALB* (NM_000477) gene were used to normalize the data and to control for potential contamination of cDNAs by genomic DNA. Primer sequences are available elsewhere[1]. The quantitative data are the means ± Standard Deviation (SD) of three experimental replicates and these are presented as ratios among values for individual mRNAs. The significance of variations among samples was determined using a Mann-Whitney statistic test. The graph shows no statistically significant reduction in *TUBB4B* mRNA abundance in affected individuals compared to controls C1, C2, C3 (regrouped in C). Data are presented as mean ± SEM. n.s.: non-significant.

(**B**) Appearance of steady-state, depolymerizing and repolymerizing microtubules in fibroblasts from control (C1, C2, C3) and affected (P1, P2, P3) individuals. Fibroblasts were directly fixed in ice-cold methanol (5 min. at −20 °C; steady-state MT lattice), maintained on ice for 30 min. (complete MT depolymerization) and fixed, or maintained on ice for 30 min. and incubated at 37°C (MT repolymerization) for 6, 8 or 10 min. and fixed. Fixed cells were permeabilized (1 hour, room temperature) and stained using a mouse Anti-EB1 primary antibody (1:200, overnight, 4°C; BD Biosciences) and an Alexa-Fluor 488– conjugated goat anti-mouse IgG (1:1,000; 1 hour, room temperature; Life Technologies ThermoFisher Scientific). A mounting medium containing DAPI (Prolong Gold, Life Technologies ThermoFisher Scientific) was used to label nuclei. Immunofluorescence images were obtained using a Spinning Disk Zeiss microscope (Zeiss). The final images were generated using ImageJ (National Institutes of Health, Bethesda, MA).

(**C**) The individual distance of EB1 relative to the centrosome determined using Icy software is plotted as a dot, with the mean distance represented by a horizontal line. Statistical analyses were carried out by analysis of variance (ANOVA) and the PLSD Fisher test. ****: p-value < 0.0001; n.s.: non-significant p-value ≥ 0.5. The control value C is the mean of values from C1, C2 and C3. ****: p-value < 0.0001.

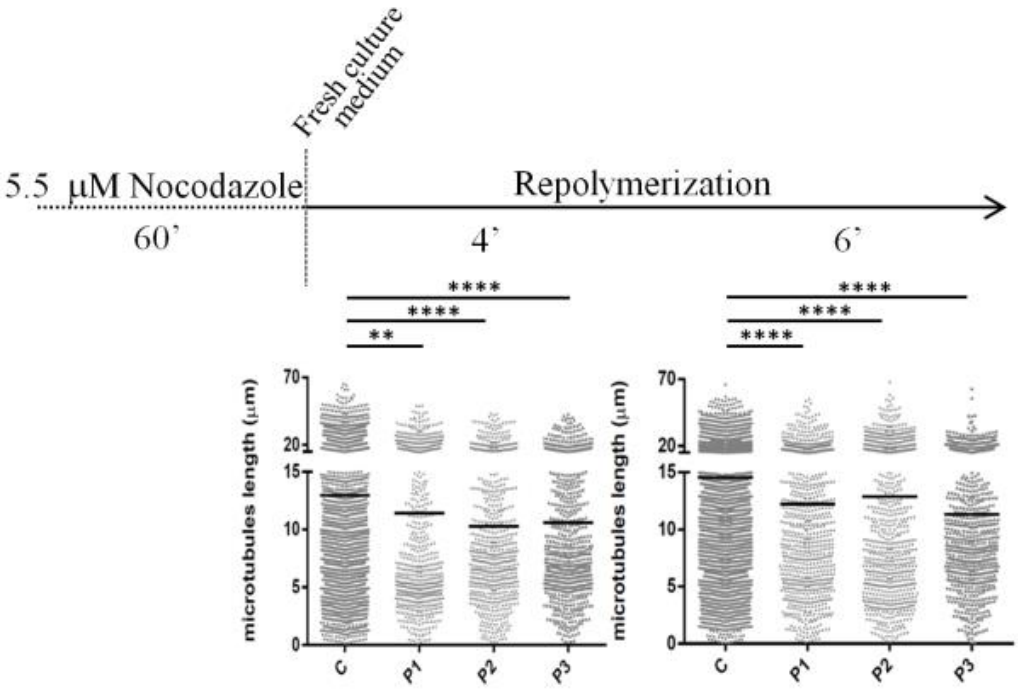

Figure S4. *TUBB4B* c.1172G>A and c.1171C>T mutations affect the rate of growth of patient fibroblast MTs after complete deploymerization with nocodazole. Fibroblasts were incubated for 60 min. in 5.5 µM nocodazole before fixation and further treatment and staining as described in Figure S2. The length of individual repolymerizing microtubules was measured from EB1 to the centrosome using Icy software and is plotted as a dot, with the mean distance represented by a horizontal line. Statistical analyses were carried out by analysis of variance (ANOVA) and the PLSD Fisher test. **: p-value <0.01; ****: p-value < 0.0001; n.s.: non-significant p-value ≥ 0.5.

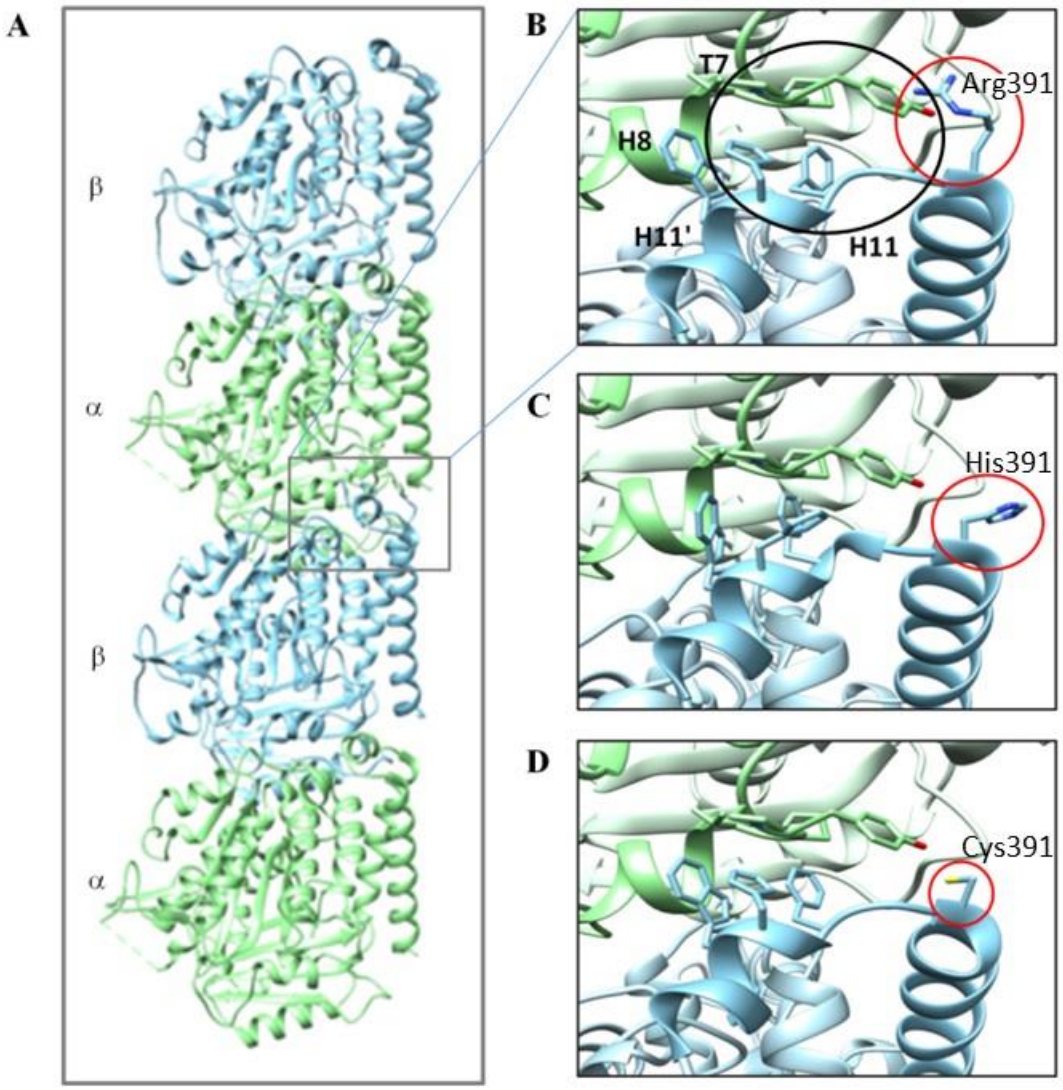

Figure S5. Predicted TUBB4B conformational changes induced by p.Arg391Cys and p.Arg391His substitutions. The structure of the end of the H11 helix in β-tubulin-bound α-tubulin (β-tubulin in blue, α-tubulin in green) is shown. The figures were generated with I-Tasser. Predicted models were aligned on the cryo-electron microscopy structure of a GDP-protofilament (GDP-K MT, EMD-6353, PDB: 3JAS) using UCSF Chimera software.[2-4]

(**A**) Overview of αβ-tubulin heterodimers within an assembled microtubule.

(**B**) The p.Arg391 residue at the end of helix H11 in β-tubulin contributes to a binding pocket that interacts with α-tubulin in the longitudinally adjacent heterodimer.

(**C, D**) The p.Arg391His (**C**) and p.Arg391Cys (**D**) substitutions were introduced to show their respective effects on the binding pocket.

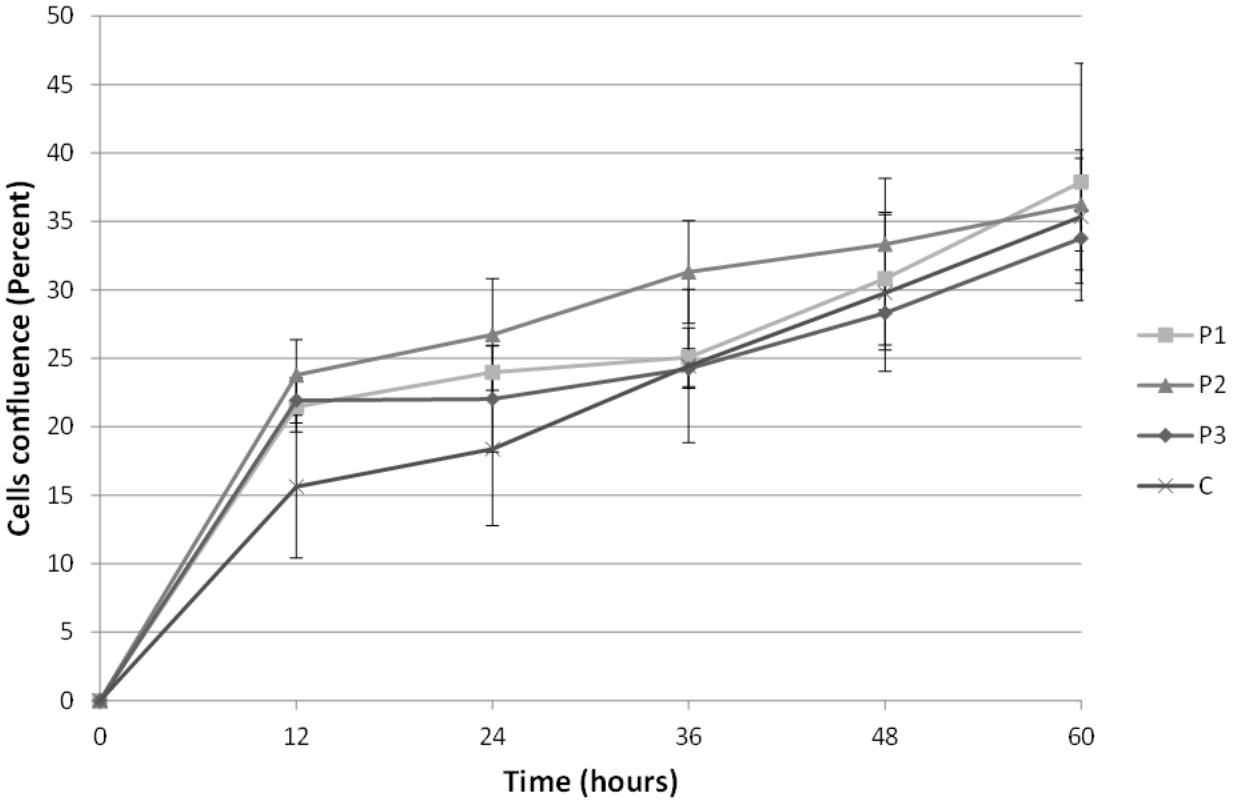

Figure S6. TUBB4B p.Arg391Cys and p.Arg391His substitutions do not affect fibroblast proliferation as determined by a live cell proliferation assay. A real time cell analyzer (RTCA) xCELLigence (ACEA Bioscience Inc., San Diego, CA) was used to monitor fibroblast cell proliferation based on impedance measurements. Cells (n= 1350 per well) were seeded in 96-well E-plates (ACEA Bioscience Inc.) contained in Opti-MEM Glutamax I medium (Life Technologies ThermoFisher Scientific) supplemented with 10% fetal bovine serum (Life Technologies ThermoFisher Scientific) and 1% streptomycin/penicillin (Life Technologies ThermoFisher Scientific). Variations in the impedance signal, expressed as cell index (CI), was recorded at 37 °C, 5% CO_2 every 12 hours for 5 days. CI were measured for each cell line and culture condition in triplicate. The cell doubling time (CDT) was determined in each well using RTCA software v1.2.1. The significance of CDT variations among samples was determined using a Mann-Whitney statistic test. Data are presented as mean ± SD.

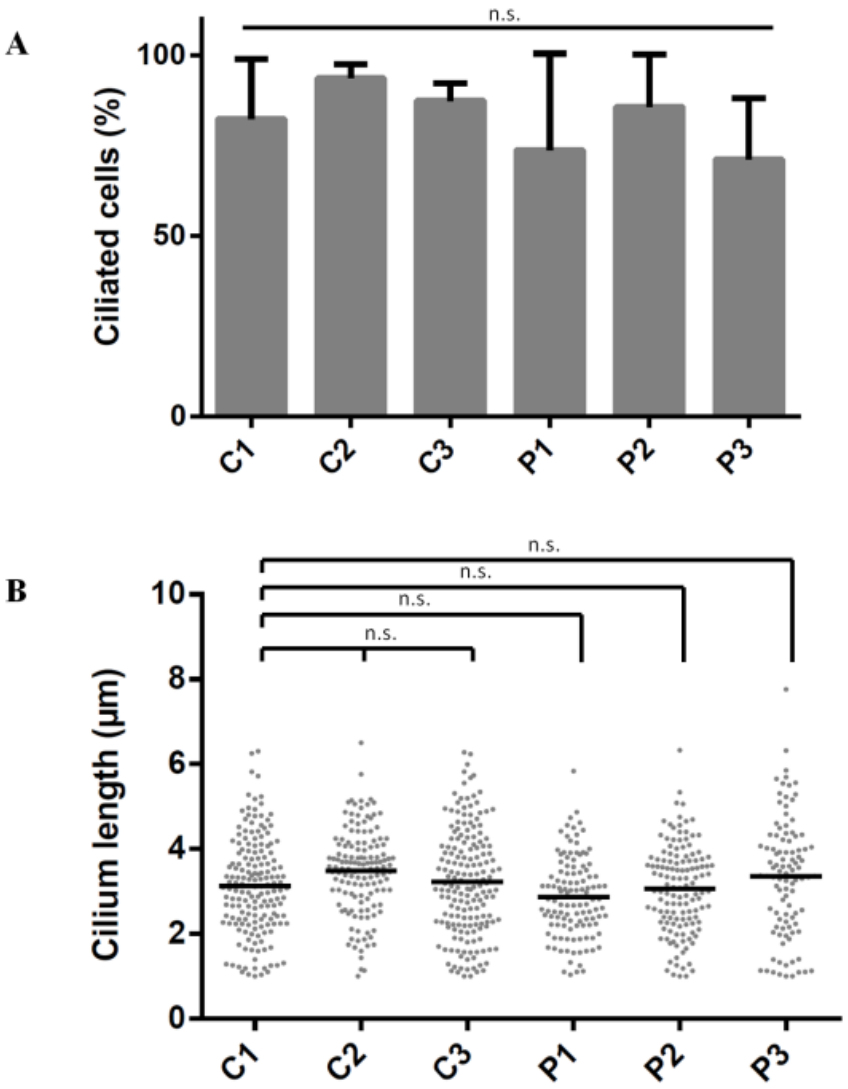

Figure S7. TUBB4B p.Arg391Cys and p.Arg391His substitutions do not affect fibroblast ciliogenesis. Immunofluorescence staining and cilia length measurements in cultured human fibroblasts from healthy (C1, C2, C3) and affected (P1, P2, P3) individuals were performed as described previously.[5-6]

(**A**) The proportion of fibroblasts containing a primary cilium was calculated by examining at least 100 cells in at least four fields from two independent experiments. Data are presented as mean ± SD.

(**B**) The length of individual primary cilia among > 100 ciliated cells from C1, C2, C3, P1, P2 and P3, respectively, is plotted as a dot, with the mean distance represented by a horizontal line. n.s.: non-significant $p \geq 0.5$.

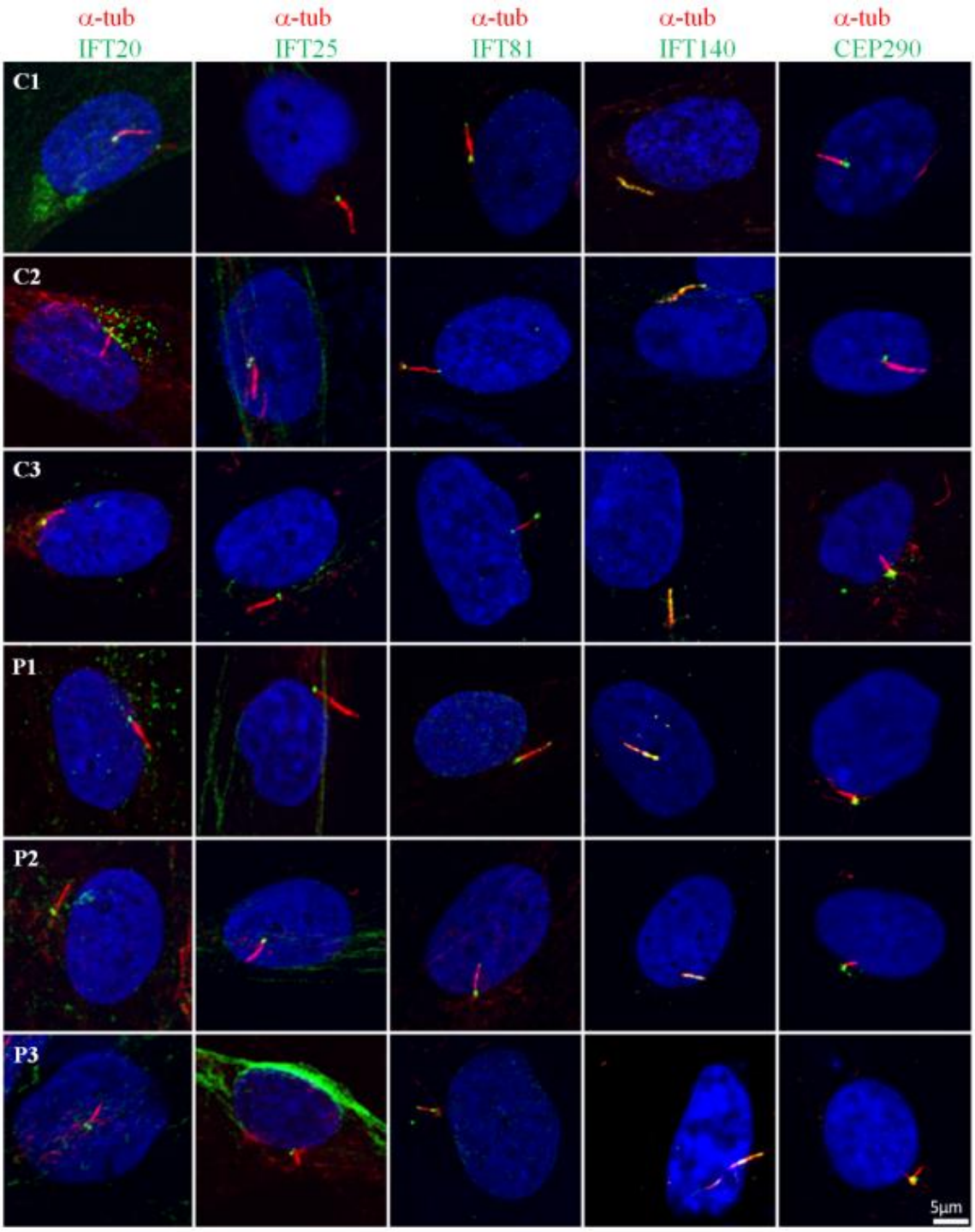

Figure S8. TUBB4B p.Arg391Cys and p.Arg391His substitutions do not affect the localization of the intraflagellar transport IFT20, IFT25, IFT81, IFT140 proteins or the centrosomal CEP290 protein in the fibroblasts of affected individuals. Immunofluorescence staining was performed in cultured human fibroblasts from healthy control (C1, C2, C3) and affected (P1, P2, P3) individuals as described previously.[5-6] Ciliary axonemes were stained using mouse monoclonal anti-acetylated α-tubulin (red). Ciliary signals obtained using antibodies to IFT20, IFT25, IFT81, IFT140 and CEP290 (green) did not show any significant difference among >20 ciliated control and mutant cells.

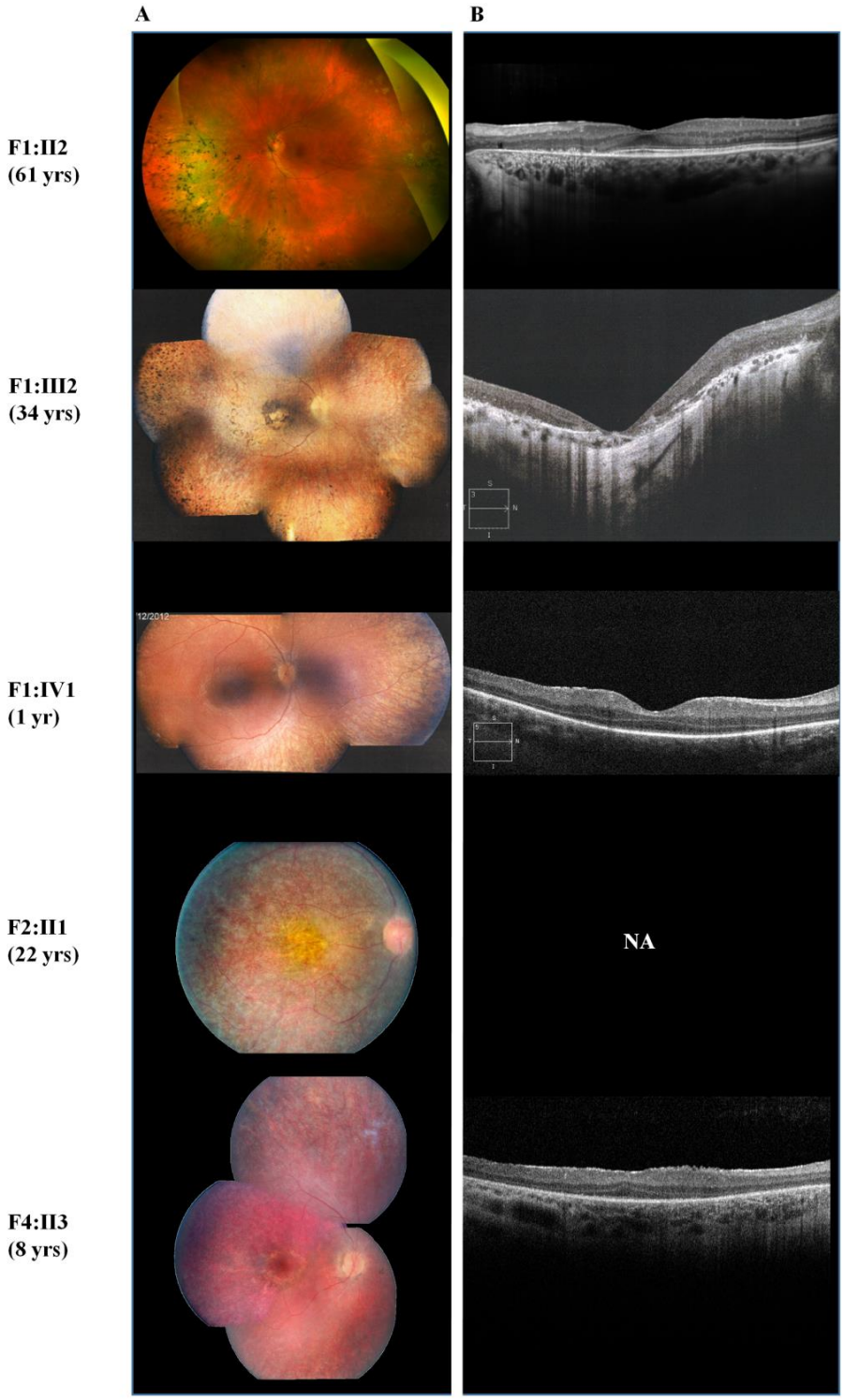

Figure S9. Representative fundus and optic coherence tomography (OCT) in individuals with TUBB4B substitutions affecting p.Arg391. (**A**) Right eye fundi showing thin retinal vessels, salt and pepper appearance of the posterior pole, yellowish peripheral retina with round pigmented spots at the fundus in F1:II2 and F1:III1 and macular reorganization in F1:II2. (**B**) Right eye spectral domain OCT revealing marked alteration of the retinal structure in F1:II2 and relatively preserved outer retina in the foveal and parafoveal area but not outside the central region in F1:III1 and F4:II3.

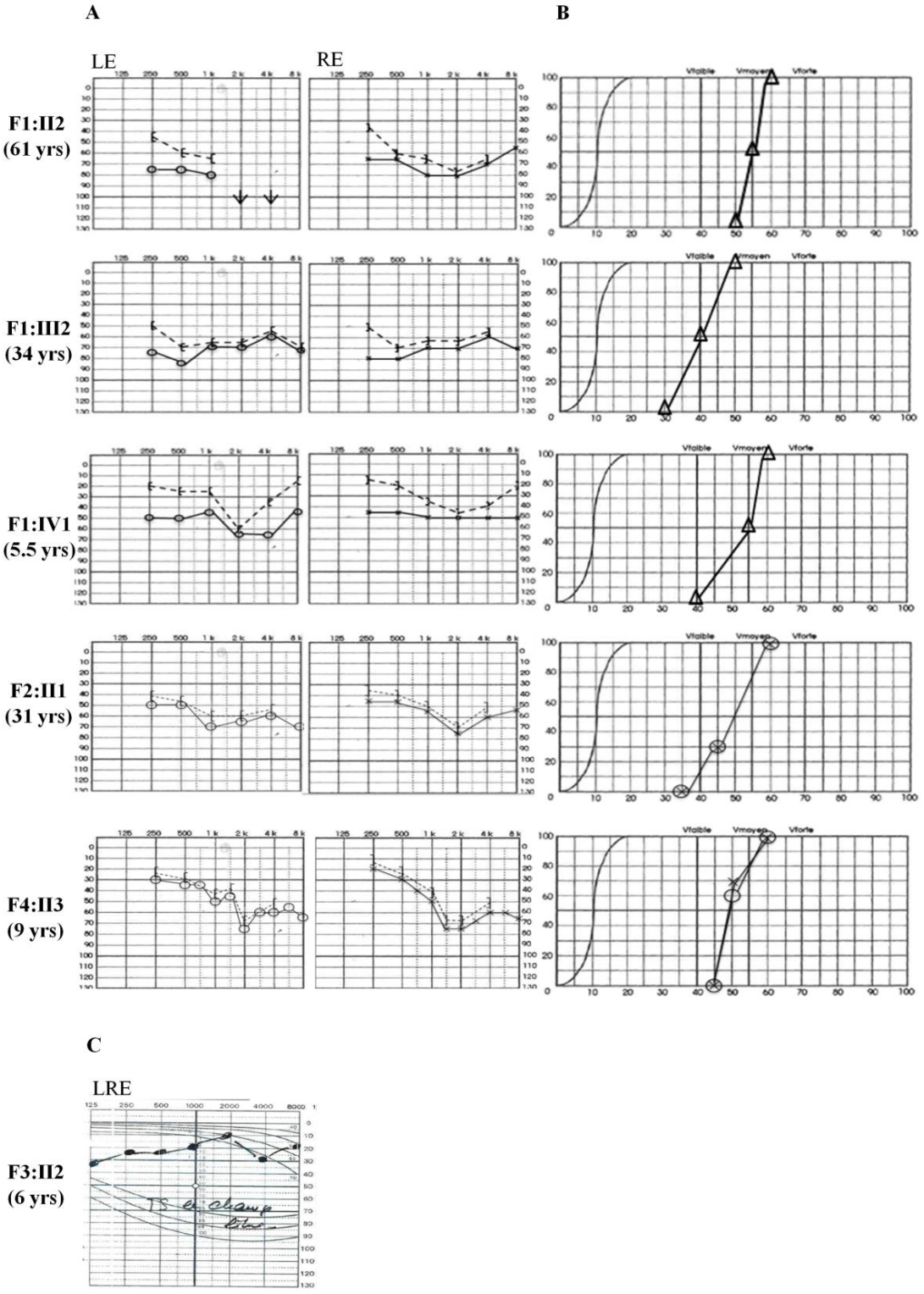

Figure S10. Representative auditory defects in individuals with TUBB4B substitutions affecting p.Arg391. (**A**) Pure Tone Audiometry using Air Sound conduction (circles) and Bone Sound conduction (crosses). (**B**) Speech Audiometry. (**C**) Free field Air conduction Thresholds. LE: Left ear, RE: Right ear, LRE: left and right ears. (yrs: years).

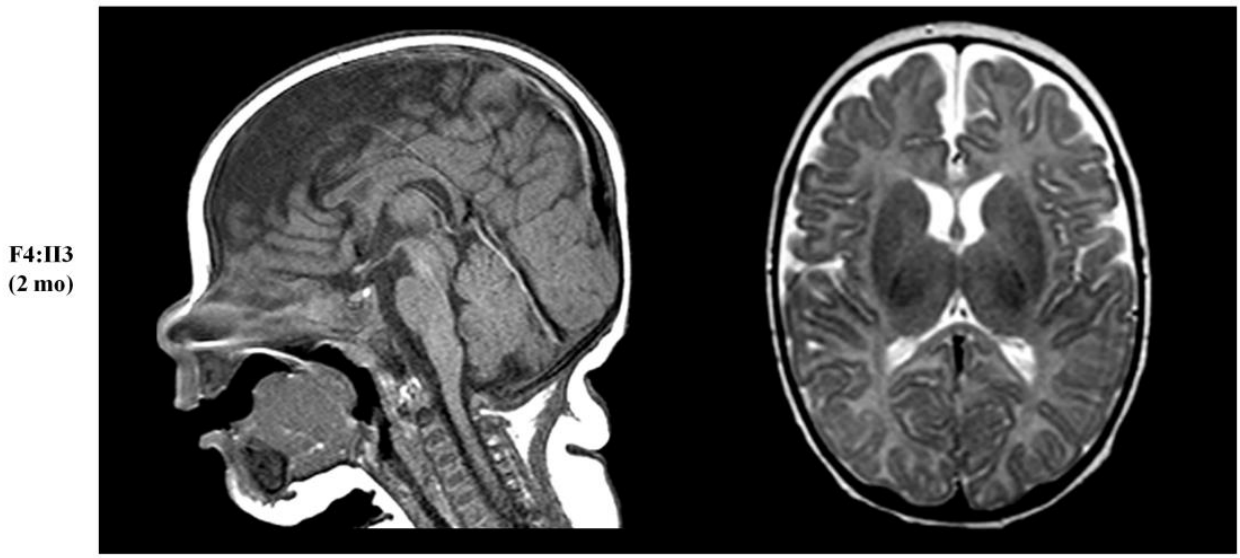

Figure S11. Brain MRI. Sagittal T1 weighted MRI (Left panel) and Right Axial T2 weighted image (right panel) showing normal cortical gyration and brain anatomy. The age of the affected individual at examination is given in parentheses (mo: months).

A

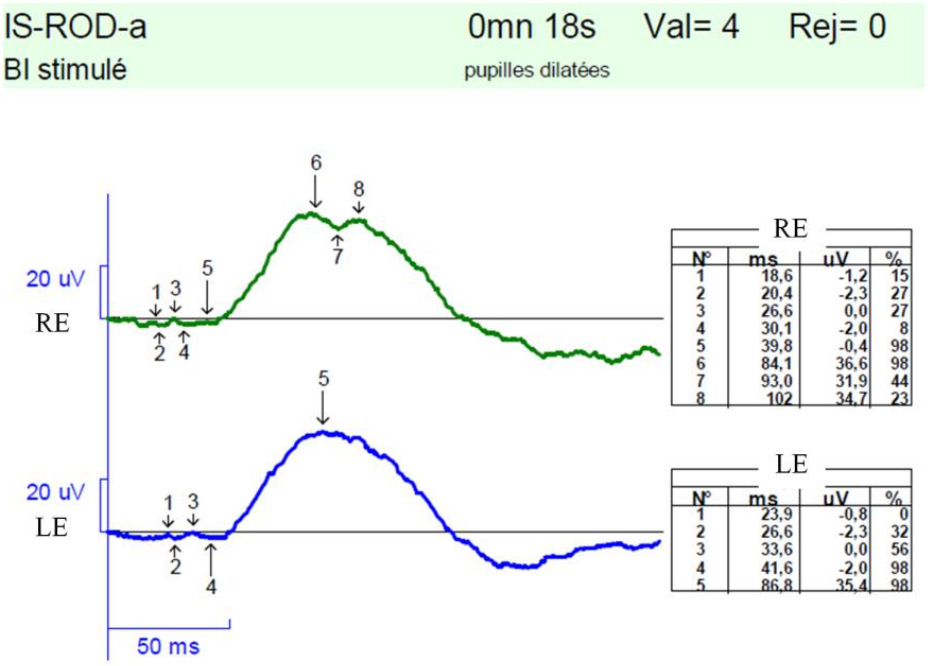

B

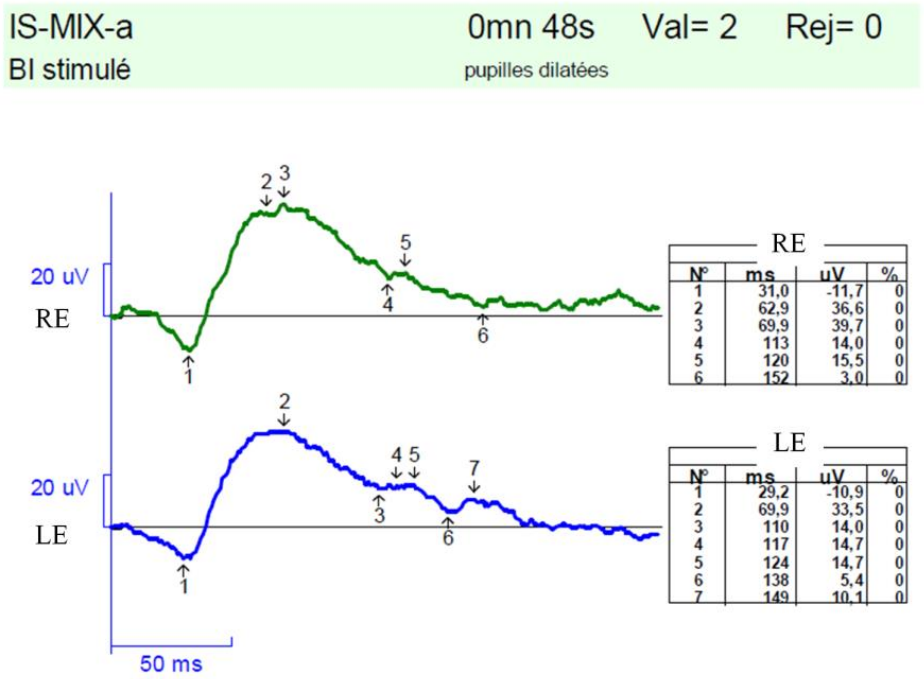

Figure S12. Electroretinogram responses of the right and left eyes (RE and LE, respectively) of subject F1:II.2 carrying the c.1172G>A mutation on 29% of *TUBB4B* alleles. (A) Flash-ERG ROD response: amplitude and morphology of waves are normal. **(B)** Flash-ERG Mixed response: amplitude and morphology of waves are normal.

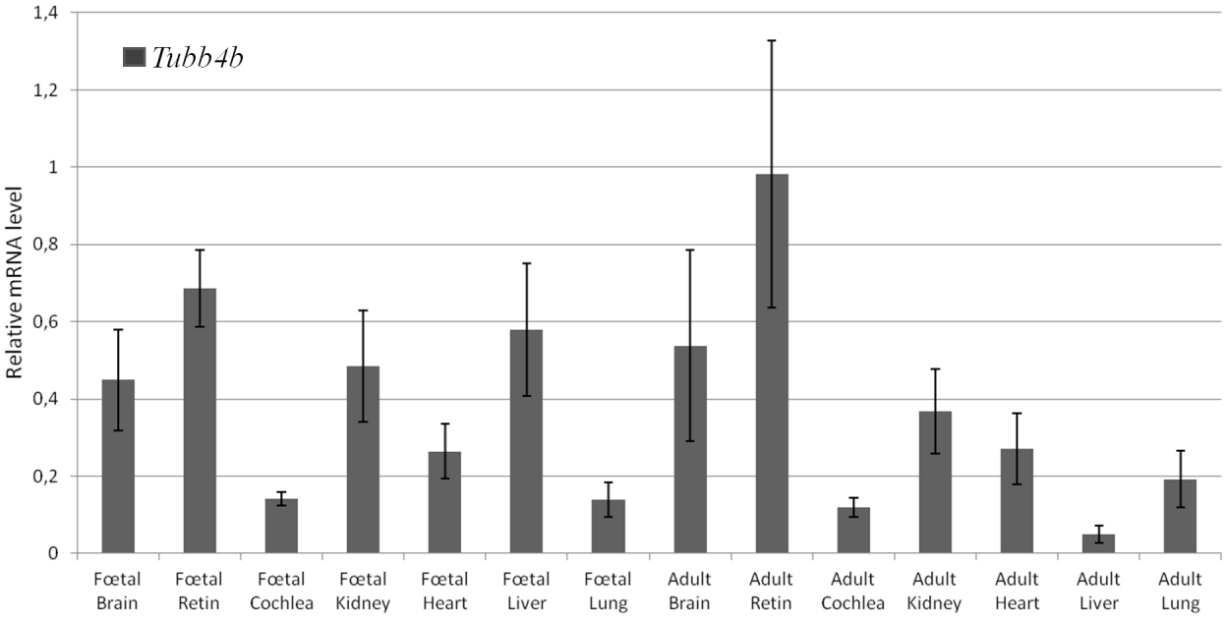

Figure S13. RTqPCR expression analysis of *tubb4b* mRNA in embryonic and adult mouse tissues showing high retinal but not cochlear *tubb4b* expression. *tubb4b* mRNA was amplified as a 64 bp fragment using exonic primers: (forward, 5'-3') cgaagccaccggtggcaa and (reverse, 5'-3') catggtgccgggctccaa. *B2m*, *Hprt1*, *Rplp0* mRNAs and the *Alb* gene primers were used to normalize the data and to control for the absence of contamination of cDNAs by genomic DNA. Primer sequences are available elsewhere.[7] Data are presented as mean ± SEM from three independent experiments.

Table S1. Whole exome resequencing coverage and read-depth.

		Coverage		
Family	**Individual**	**Mean**	**15X**	**30X**
1	II1	103.2	98.7	94.2
	II2	188.4	96.7	96
	III2	172.9	99.4	98.4
	IV1	155.1	96.8	95.7
2	I1	123	96.6	94.8
	I2	141.1	96.6	95.4
	II1	129.8	96.7	95.3
3	I1	128.8	96.6	95.1
	I2	132.4	96.5	95.1
	II2	178.3	99.3	98.3
4	I1	156.8	98.6	97.1
	I2	189.6	98.5	97.5
	II3	211.5	98.8	98

Table S2. Whole exome resequencing data. Exhaustive list of rare SNVs/indels and *de novo* and recessive variants identified in the four families. The deleterious effect of variants was assessed using the Alamut Mutation Interpretation software which uses Polyphen 2, SIFT, Mutation Taster, GVGD, SpliceSiteFinder-like, MaxEntScan, NNSPLICE and/or Human Splicing Finder. MAF: minor allele frequency.

Provided as an excel file

Table S3. PCR-based deep sequencing of *TUBB4B* exon 4 identifies mosaicism and *de novo* mutations. The quantification of the ratio of mutant to wild-type sequence reads is presented for all affected individuals and their parents.

Family	Individual	Total number of reads	Number of wild-type reads	Number of mutant reads	Percentage of mutant alleles
F1	II-1	2000	1991 G	5 A	0.25
	II-2	1956	1386 G	570 A	29.1
	III-1	2087	2087 G	0 A	0
	III-2	2215	1147 G	1063 A	47.9
F2	I-1	1712	1712 G	0 A	0
	I-2	1891	1644 G	245 A	12.9
F3	I-1	1997	1995 G	2 A	0.1
	I-2	2258	2254 G	3 A	0.13
F4	I-1	2225	2223 C	2 T	0.09
	I-2	1998	1995 C	2 T	0.1

Table S4. Oligonucleotides used for PCR and Sanger sequencing.

Exon	Orientation	Sequence (5'-3')
1	*forward*	ggcaaggccaatcaaacgag
	reverse	tgctcatcgctgatcacctc
2	*forward*	caaattcggcgccaaggtaa
	reverse	cacggctcaccgaaaacg
3	*forward*	gcgtcccttgtagttttggga
	reverse	gagcagccccttgacctttg
4	*forward*	gtggtcagctcacaccatgt
	reverse	aggaatgggcaaagcgaaac

References.

1. Gerard, X., Perrault, I., Hanein, S., Silva, E., Bigot, K., Defoort-Dellhemmes, S., Rio, M., Munnich, A., Scherman, D., Kaplan, J., Kichler, A., Rozet, J.M. (2012). AON-mediated Exon Skipping Restores Ciliation in Fibroblasts Harboring the Common Leber Congenital Amaurosis CEP290 Mutation. Mol. Ther. Nucleic Acids. *1*, e29.
2. Pettersen, E.F., Goddard, T.D., Huang, C.C., Couch, G.S., Greenblatt, D.M., Meng, E.C., Ferrin, T.E. (2004). UCSF Chimera--a visualization system for exploratory research and analysis. J. Comput. Chem. *25*, 1605-12.
3. Yang, J., Yan, R., Roy, A., Xu, D., Poisson, J., Zhang, Y. (2015). The I-TASSER Suite: protein structure and function prediction. Nat. Methods *12*, 7-8.
4. Zhang, R., Alushin, G.M., Brown, A., Nogales, E. (2015). Mechanistic Origin of Microtubule Dynamic Instability and Its Modulation by EB Proteins. Cell *162*, 849-59.
5. Perrault, I., Halbritter, J., Porath, J.D., Gérard, X., Braun, D.A., Gee, H.Y., Fathy, H.M., Saunier, S., Cormier-Daire, V., Thomas, S., Attié-Bitach, T., Boddaert, N., Taschner, M., Schueler, M., Lorentzen, E., Lifton, R.P., Lawson, J.A., Garfa-Traore, M., Otto, E.A., Bastin, P., Caillaud, C., Kaplan, J., Rozet, J.M., Hildebrandt, F. (2015). IFT81, encoding an IFT-B core protein, as a very rare cause of a ciliopathy phenotype. J. Med. Genet. *52*, 657-65.
6. Perrault, I., Saunier, S., Hanein, S., Filhol, E., Bizet, A.A., Collins, F., Salih, M.A., Gerber, S., Delphin, N., Bigot, K., Orssaud, C., Silva, E., Baudouin, V., Oud, M.M., Shannon, N., Le Merrer, M., Roche, O., Pietrement, C., Goumid, J., Baumann, C., Bole-Feysot, C., Nitschke, P., Zahrate, M., Beales, P., Arts, H.H., Munnich, A., Kaplan, J., Antignac, C., Cormier-Daire, V., Rozet, J.M. (2012). Mainzer-Saldino syndrome is a ciliopathy caused by IFT140 mutations. Am. J. Hum. Genet. *90*, 864-70.
7. Gerard X, Perrault I, Munnich A, Kaplan J, Rozet JM. (2015). Intravitreal Injection of Splice-switching Oligonucleotides to Manipulate Splicing in Retinal Cells. Mol. Ther. Nucleic Acids. *4*, e250.